STEELS FOR GENERAL ENGINEERING PURPOSES

EFFECT OF TEMPERING TEMPERATURE ON THE STRUCTURE AND MECHANICAL PROPERTIES OF MEDIUM-CARBON STEEL WITH ELEVATED SILICON CONTENT

S. I. Borisov,[1, 2] Yu. I. Borisova,[1, 2] E. S. Tkachev,[1, 2] T. V. Knyazyuk,[3] S. M. Gaidar,[1] and R. O. Kaibyshev[1]

The effect of quenching and tempering on the microstructure, phase composition and mechanical properties of steel 0.33C – 1.8Si – 1.44Mn – 0.58Cr is investigated. The structure is studied using scanning and transmission electron microscopy, dilatometry and differential scanning calorimetry. Tensile and impact strength tests are performed. The Rockwell hardness is measured. The processes of formation of carbides in the steel at different temperatures are analyzed, as well as the influence of the structure on the mechanical properties. Quenching yields laths of martensite with carbon-saturated dislocation boundaries due to formation of Cottrell atmospheres. The internal stresses reach 40% of the yield strength $\sigma_{0.2}$. Tempering to a temperature of 280°C causes precipitation of transition η-carbides (Fe_2C) inside the laths, which depletes the martensite matrix of carbon by about 90%. This increases the yield strength by 16% to 1130 MPa despite the lowering of the internal stresses and growth of the width of the laths. Precipitation of cementite chains over the lath and block boundaries occurs in tempering at 500°C, which is accompanied by lowering of the yield strength to 1130 MPa. Calculations of the proportion of carbon atoms in the martensite shows that almost all of the carbon present in the steel goes to formation of cementite. The decomposition of martensite during tempering increases the toughness but has a minor effect on the strength-ductility parameter $\sigma_r \times \delta$ (MPa · %).

Key words: mechanical properties, martensitic structure, quenching and tempering.

INTRODUCTION

Development of the building industry, transport and agricultural machinery requires low-alloy steels combining a high yield strength ($\sigma_{0.2} \geq 1000$ MPa) with enough ductility ($\delta \geq 10\%$) and impact toughness ($KCV \geq 40$ J/cm^2) [1, 2]. Such properties can be obtained by creating novel high-strength low-alloy steels and optimizing their chemical composition with the aim to form a structure represented by tempered martensite, retained austenite and particles of transition carbides [1, 2].

Application of interrupted quenching to low- and medium-carbon steels provides elevation of their ductility and impact toughness due to formation of a lath martensite structure with controlled fractions of retained austenite stabilized by precipitation of carbon from the martensite [1 – 3]. The main feature of recent high-strength steels is an elevated content of Si and Mn. Alloying with silicon helps to suppress precipitation of cementite and to decelerate the decomposition of austenite in the range of 180 – 400°C [4]. Manganese improves the hardenability by decelerating the decomposi-

[1] Russian State Agrarian University – Moscow Timiryazev Agricultural Academy, Moscow, Russia (e-mail: borisov_si@bsu.edu.ru).
[2] Belgorod State National Research University, Belgorod, Russia.
[3] National Research Center "Kurchatov Institute" – Central Research Institute of Structural Materials "Prometey," St. Petersburg, Russia.

tion of austenite under accelerated cooling and hence lowering the transformation temperature and stabilizes the retained austenite under heating to 400°C [4, 5]. It is known that Mn, Cr and Mo reduce the diffusion mobility of carbon in ferrite. Therefore, the regions of the microstructure enriched with these elements tend to attract carbon [4]. Silicon and molybdenum are strong solid-solution hardeners of ferrite [5].

As a rule, the combination of strength and ductility is described in terms of the product $\sigma_r \times \delta$ (MPa · %). This parameter is used to evaluate the stamping ability of high-strength steels and their resistance to fracture, because it is quite difficult to study the impact toughness in thin rolled sheets from automotive steels [1]. However, it has been shown in [6] that in the general case there is no correlation between parameter $\sigma_r \times \delta$ and the impact toughness for steels subjected to interrupted quenching. It is quite interesting to determine the effect of the structural changes under tempering on the combination of the impact toughness, strength and ductility of low-alloy steels with an elevated content of silicon, because this should allow us to assess the economic viability of such treatment for manufacturing hot-rolled sheets with a thickness exceeding 10 mm. For this reason, we have made an analysis of the mechanical properties measured in tensile tests of a steel and of the impact toughness of the steel.

The aim of the present work was to study the evolution of the structure and the variation of the mechanical properties under tempering for a medium-carbon steel with an elevated silicon content.

METHODS OF STUDY

The steel studied had the following chemical composition (in wt.%): 0.33 C, 1.85 Si, 1.44 Mn, 058 Cr, 0.0084 Ni, ≤ 0.007 S, ≤ 0.01 P, the remainder Fe. The steel was melted in an open induction furnace and then subjected to electroslag remelting. The ingot obtained was homogenized at 1150°C for 4 h, forged at 1150 – 1000°C and cooled in air. The billets cut from the ingot were heated to 900°C with a hold for 30 min for complete austenitization and then quenched in heated water and tempered at 200, 280, 400 and 500°C for 1 h with subsequent air cooling.

The specimens for scanning electron microscopy (SEM) were prepared by electropolishing; the foils for transmission electron microscopy (TEM) were obtained by double-jet electropolishing in a solution of 10% $HClO_4$ in CH_2COOH. The foils were studied using a JEOL JEM-2100 transmission electron microscope.

The misorientation maps of were plotted using a FEI Quanta 600 FEG scanning electron microscope by the method of EBSD and a EDAX VelocityTM camera. The fracture surfaces were studied using the same microscope. The original austenite grains, packets and blocks were identified by the methods described in [7]. The dislocation density was determined by counting individual dislocations coming

out to the surface of the foil using TEM [7, 8]. The dislocation density was also counted using the maps of the distribution of orientations obtained by EBSD [7, 8], i.e.,

$$\rho_{KAM} = 2\theta_{KAM}/bh, \qquad (1)$$

where θ_{KAM} is the average misorientation between neighbor points in the map of the distribution of orientations at scanning step h, and $b = 0.25$ nm is the Burgers vector in ferrite [7].

The tensile tests were carried out for flat specimens with 35-mm length of the functional part and cross section 7×3 mm using an Instron 5882 device at deformation speed 1 mm/min. The Rockwell hardness HRC was measured using a WolpertWilson 600 RD hardness tester. The impact toughness *KCV* was determined for standard V-notched specimens with working section 10×8 mm and length 55 mm using an Instron IMP460 pendulum impact machine. The specific volume of retained austenite was assessed by the method of magnetic saturation using a FERITSCOPE FMP30 device.

The differential scanning calorimetry (DSC) was performed using an SDT Q600 TA Instruments device in an atmosphere of argon. The specimens with a mass of 50 mg were heated at a rate of 10 K/min. Before the DSC, the specimens were quenched from 900°C. The dilatometric tests were performed for cylindrical specimens with a length of 10 mm and a diameter of 3 mm using a DIL 805 TA Instruments quenching dilatometer. The dilatometric curve was obtained in cooling from 900°C to room temperature at a rate of 50 K/sec.

RESULTS AND DISCUSSION

The critical temperatures $Ac_1 = 758$°C and $Ac_3 = 817$°C for the steel were determined in calorimetric tests. These data were used to choose the temperature of heating for quenching (900°C), which provided complete austenitization of the steel. The dilatometric studies allowed us to determine the points of the martensitic transformation, i.e., $M_s = 325$°C and $M_f = 104$°C. It follows from these data that water quenching gives a fully martensitic structure with an inconsiderable content of retained austenite.

According to the SEM data (Fig. 1), the steel acquires a homogeneous structure typical for packet martensite after the quenching. Figure 2 presents the results of the analysis of the misorientation patterns and of the fine structure of the steel after quenching. The structure after the quenching from 900°C is typical for packet martensite and consists of original austenite grains (OAG), packets, blocks and laths (Fig. 2*a*, Table 1) [10]. The retained austenite has the form of thin layers arranged over the boundaries of the OAG and packets. We may speak of the following features of the structure of the steel: (*1*) the distance between high-angle boundaries is about equal to the width of the blocks, i.e., most of the block boundaries are high-angle ones; (*2*) the size of the
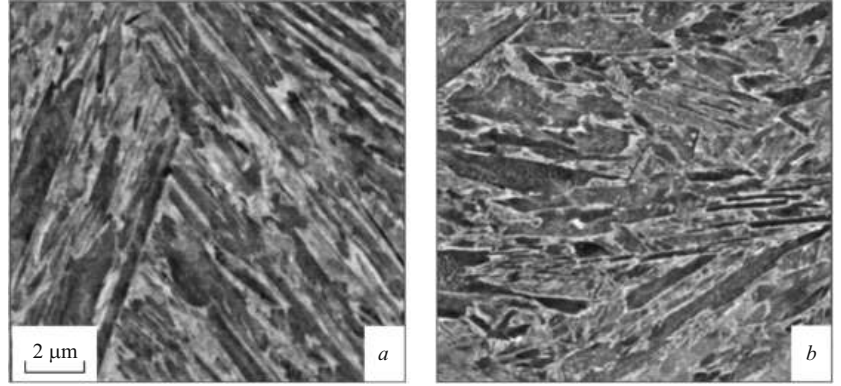
Fig. 1. Structure of medium-carbon steel (SEM) after quenching from 900°C (30 min) (*a*) and quenching and tempering at 280°C (*b*).

OAG is almost 30 times larger than the distance between the high-angle boundaries. The OAG with a size of ≥ 25 μm contain 6 or 7 packets; the OAG with a size of ≤ 20 μm consist of one large packet and one or two blocks composing a packet with a smaller size. The experimentally determined proportion of the sizes of the packets and of the OAG is $D_{pack} \approx 0.12 D_{OAG}$; the proportion of the sizes of the blocks and of the packets $d_{bl} \approx 0.25 D_{pack}$ (Table 1). We know of the following dependences between the parameters of the structure of lath martensite [7, 11]:

$$D_{pack} = \sqrt{\frac{3\sqrt{3}}{8N_{pack}}} D_{OAG}, \qquad (2)$$

$$d_{bl} = \frac{1}{N_{bl}} D_{pack}, \qquad (3)$$

where N_{pack} is the number of packets in the OAG and N_{bl} is the number of blocks in the packet.

Equation (2) is not obeyed for the steel studied, whereas the observed proportion of the sizes of packets and blocks correlates well with Eq. (3). This is connected with the fact that regions with an almost equiaxed shape where the blocks belong to other equivalent habit planes $\{111\}_\gamma$ appear in the

OAG in addition to the regions belonging to one habit plane $\{111\}_\gamma$ under the $\gamma \rightarrow \alpha'$ transformation. In their turn, these regions are divided into rectangular blocks, which is responsible for the low distance between the high-angle boundaries (Table 1). The number of the packets and their shape depend strongly of D_{OAG}. At $D_{OAG} \leq 20$ μm, the number of the regions with blocks belonging to different martensite packets decreases to $1 - 2$. Consequently, the disintegration of the OAG in the medium-carbon steel makes it possible to pass from the four-level hierarchic system of the structure of packet martensite [10] to a three-level one, i.e., OAG, blocks and laths. Therefore, it can be assumed that direct proportionality between the sizes of the packets and of the OAG is obeyed only for the steel containing ≤ 0.25 wt.% carbon [7, 11].

The third special feature of the structure of the steel is a little width of the laths (Table 1), which is almost 25% less than in the steel with 0.25% C [7]. It is known [11] that the width of the martensite laths does not depend on the size of the OAG and of the packets and is determined by the deformation of the lattice under the $\gamma \rightarrow \alpha'$ transformation and by the segregations of carbon on their boundaries. The lath boundaries are sources of high elastic stresses that correlate with the dislocation density ρ_{KAM}. The value of ρ_{KAM} is
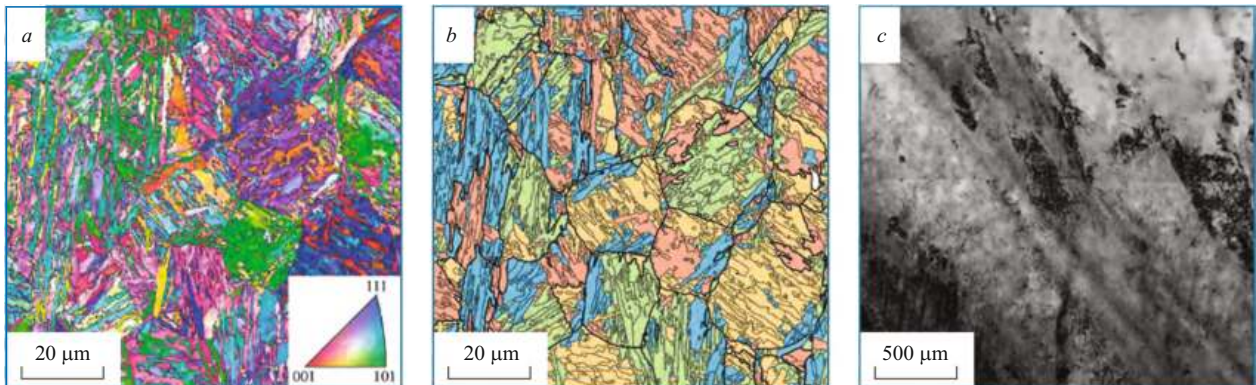
Fig. 2. Post-quenching structure of medium-carbon steel revealed by EBSD analysis (*a*) and TEM (*c*) and reconstructed packets of lath martensite (*b*).

TABLE 1. Parameters of Microstructure after Tempering at Different Temperatures

T_{temp}, °C	d_{pack}, μm	d_{bl}, μm	l_{av}, μm	h_1, μm	ρ_{TEM}, m$^{-2} \times 10^{14}$	θ_{KAM}, deg	ρ_{KAM}, m$^{-2} \times 10^{14}$	σ_{int}, MPa	d_p, nm	V_{aust}, %
Ini.	2.8 ± 0.5	0.6 ± 0.2	0.8 ± 0.2	175 ± 20	2.7 ± 0.6	1.07	10.1	470	–	1.6 ± 0.1
200	3.7 ± 0.6	0.9 ± 0.2	1.2 ± 0.2	190 ± 15	2.7 ± 0.7	0.83	7.82	414	60/7	1.6 ± 0.3
280	3.1 ± 0.5	0.7 ± 0.2	1.2 ± 0.2	205 ± 25	2.6 ± 0.4	0.92	8.62	435	71/13	0.6 ± 0.5
400	3.0 ± 0.5	0.6 ± 0.2	1.0 ± 0.2	215 ± 20	2.1 ± 0.5	0.76	7.18	397	104/13	0
500	4.2 ± 0.6	1.0 ± 0.2	1.5 ± 0.2	230 ± 30	2.0 ± 0.5	0.74	6.99	391	55/29	0

Note. The size of the original austenite grains is 26.4 ± 3.3 μm.

Notations: Ini.) initial state (quenching); d_{pack}, d_{bl}) packet and block sizes, respectively; l_{av}) average distance between high-angle boundaries; h_1) lath width; ρ_{TEM} and ρ_{KAM}) dislocation density calculated by TEM and from the maps of distribution of orientations obtained by EBSD, respectively; θ_{KAM}) average misorientation in the map of distribution of orientations; σ_{int}) value of internal stresses in the steel; d_p) average particle size (length/width); V_{aust}) specific volume of retained austenite.

3 – 4 times higher than ρ_{TEM}. Accordingly, the elastic stresses from the lath boundaries, which are in fact disordered dislocation nets [12], exceed the maximum possible stresses from the lattice dislocations. The internal stresses can be evaluated using the expression [13]

$$\sigma_{int} = 0.4E \sqrt{\frac{b\,\theta_{KAM}}{h}}, \qquad (4)$$

where σ_{int} are the internal stresses and $E = 211$ GPa is the elastic modulus [11].

According to Eq. (4) the value of σ_{int} amounts to 40% of the yield strength (Tables 1 and 2). The deformation contrast on the foils studied by TEM proves the existence of high elastic stresses in the steel (Fig. 2c). The internal stresses after quenching of the steel with 0.33% C is 27% higher than in the steel with 0.25% C ($\sigma_{int} = 370$ MPa) [7]. It is known that the width of the laths after quenching grows with increase in the size of the Cottrell atmospheres and decreases with increase in the carbon concentration [11]. If we assume that the size of the Cottrell atmospheres $d_{Cot} = 7$ nm is independent of the carbon content in the steel [7, 11], a low width of the laths after quenching provides carbon segregation in the steel on lath boundaries in the required amount. The coarse blocks contain nanotwins with a length attaining 500 nm and a width not exceeding 30 nm (Fig. 2c).

Tempering of the steel does not change the sizes of the OAG and of the packets, and the structure preserves homogeneity (Fig. 1b). The sizes of the blocks grow, which results in an increase in the distance between HAB. The width of the laths and of the nanotwins increases too. The elastic stresses related to the value of ρ_{KAM} decrease. It is known that the width of the laths of packet martensite increases due to the decrease of the carbon content in Cottrell atmospheres, because carbon acquires a capacity to leave them upon growth of the temperature [11]. The dependence of the width of martensite laths on the temperature is described by the equation [11]:

$$d_{lath\ T} = d_{lath\ Q} + \lambda_0\, \chi_C^{\alpha'} \sqrt{D_{eff}\,t}, \qquad (5)$$

where $d_{lath\ T}$ is the width of the martensite laths after the tempering, $d_{lath\ Q}$ is the width of the martensite laths after the quenching, $\lambda_0 = b/d_{Cot} = 0.0357$ is the size of the diffusion barrier for the carbon atoms that have formed the Cottrell atmosphere, $\chi_C^{\alpha'}$ is the fraction of carbon atoms in the martensite, $D_{eff} = 6.2 \times 10^{-7} \exp(-Q_c/RT)$ is the diffusivity of carbon in α-Fe, $Q_c = 80$ kJ/mole, R is the universal gas constant, T is the temperature in Kelvins, and t is the tempering time.

Calculation has shown that $\chi_C^{\alpha'} = 0.107$ at.% (i.e., > 90% of the total content of carbon in the martensite) has been

TABLE 2. Mechanical Properties of Specimens of the Steel Tempered by Different Variants

| T_{temp}, °C	HRC	$\sigma_{0.2}$, MPa	σ_r, MPa	$\sigma_r/\sigma_{0.2}$	δ, %	$\sigma_r \times \delta$, MPa · %	KCV, J/cm^2
Initial[*]	54 ± 0.3	1230	1850	1.50	5.6	10,400	13
200	50 ± 0.3	1210	1670	1.38	5.8	9700	15
280	50 ± 0.5	1430	1710	1.20	6.2	10,600	19
400	48 ± 0.3	1380	1590	1.15	6.9	10,900	17
500	41 ± 0.4	1130	1230	1.09	8.9	10,900	32

[*] Quenching.
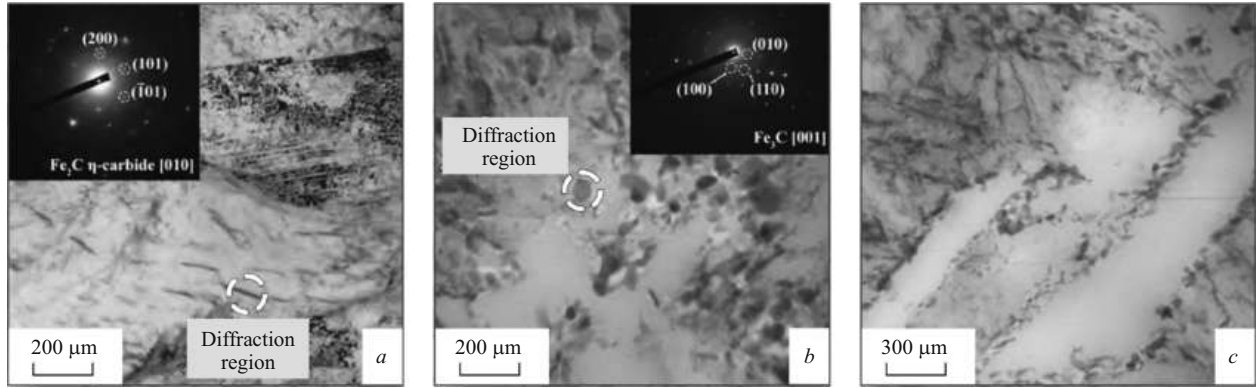
Fig. 3. Transition η-carbides in the structure of medium-carbon steel after quenching and tempering at 280°C (*a*) and particles of Fe$_3$C cementite after quenching and tempering at 500°C (*b*, *c*).

spent on formation of transition η-carbides during the tempering 280°C.

Tempering at 200°C does not affect the content of retained austenite, while the increase of the temperature to 280°C results in its almost total dissolution. After the tempering at 400°C, retained austenite has not been detected in the structure.

It should be noted that the dislocation density ρ_{TEM} remains virtually unchanged up to the tempering temperature of 400°C and decreases inconsiderably after the tempering at 500°C. The tempering at 200°C reduces ρ_{KAM} by 20%, while the elastic stresses σ_{int} decrease by 12%. The elastic stresses after the tempering at 280°C become 5% higher than after the tempering at 200°C. Elevation of the tempering temperature to 500°C lowers these stresses monotonically. The analysis of the phase composition has shown that such dependence of the elastic stresses on the tempering temperature correlates with formation of lamellar transition η-carbide (Fe$_2$C) inside the martensite laths (Fig. 3*a*). It is known that the Fe$_2$C carbide has a coherent boundary with the martensite matrix, which is a source of high elastic stresses [14]. At 500°C this carbide is substituted by round-shape cementite that forms chains over the intercrystal boundaries (Fig. 3*b* and *c*). The value of $\chi_C^{\alpha'} = 0.015$ at.% has been obtained when we analyzed Eq. (5). Consequently, the cementite forms due to carbon segregation over lath boundaries. In addition, since the cementite is a more equilibrium phase than the transition carbides, it forms both when the transition η-carbides dissolve in the martensite matrix and when the martensite is additionally depleted of carbon.

The steel studied obeys the classical stages of transformations under decomposition of martensite, i.e.,

$$\text{Martensite} \rightarrow \eta\text{-Fe}_2\text{C} \rightarrow \text{Fe}_3\text{C}. \qquad (6)$$
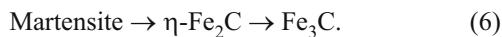
The mechanical properties of the steel after quenching and tempering are presented in Table 2. It can be seen that quenching results in a high difference between the yield strength and the ultimate strength. Tempering in the range of

280 – 400°C lowers this difference, and the ductility remains virtually unchanged. After the tempering at 500°C, the difference between $\sigma_{0.2}$ and σ_r is reduced to 9% at an almost 1.5-times increase in the ductility. Analysis of the $\sigma - \varepsilon$ curves (Fig. 4*a*) shows that strain aging does not develop in the steel studied [15, 16]. After the attainment of the yield strength, the specimens undergo a stage of strain hardening. Increase of the tempering temperature shifts the strain hardening curves ($d\sigma/d\varepsilon$) to lower degrees of deformation (Fig. 4*b*). The strain hardening decreases, which causes lowering of the ultimate strength and of the related hardness. The main structural change that can affect the deformation behavior, which is connected with the possibility of growth of the dislocation density under tension [17], is precipitation of transition η-carbides in the matrix at a tempering temperature ≤ 400°C and formation of cementite chains over lath boundaries at the tempering temperature of 500°C. Precipitation of the η-carbide raises the yield strength, while replacement of the transition carbides by a more equilibrium cementite reduces the former (Table 1).

The curves describing the dependence of the load on displacement of the pendulum under Charpy impact tests are presented in Fig. 4*c*. The values of the impact toughness, of the maximum load (P_{max}), of the dynamic ultimate tensile strength (σ_{rd}), and of the energy of nucleation (E_i) and propagation (E_p) of a crack [7, 18 – 20] are presented in Table 3. It can be seen that only point P_M of all the characteristic points is observed on the load – displacement curves [7, 18 – 20]. Increase of the tempering temperature causes growth of P_M. The load-displacement curves bear a sharp peak, where the stage of crack propagation occurs after attainment of the maximum load.

To determine the nature of the effect of heat treatment on the impact toughness, we determined the dynamic yield strength σ_{rd} according to the dependence [7, 18]:

$$\sigma_{rd} = \frac{\eta_{Pm} P_M W}{(W - a)^2 B}, \qquad (7)$$
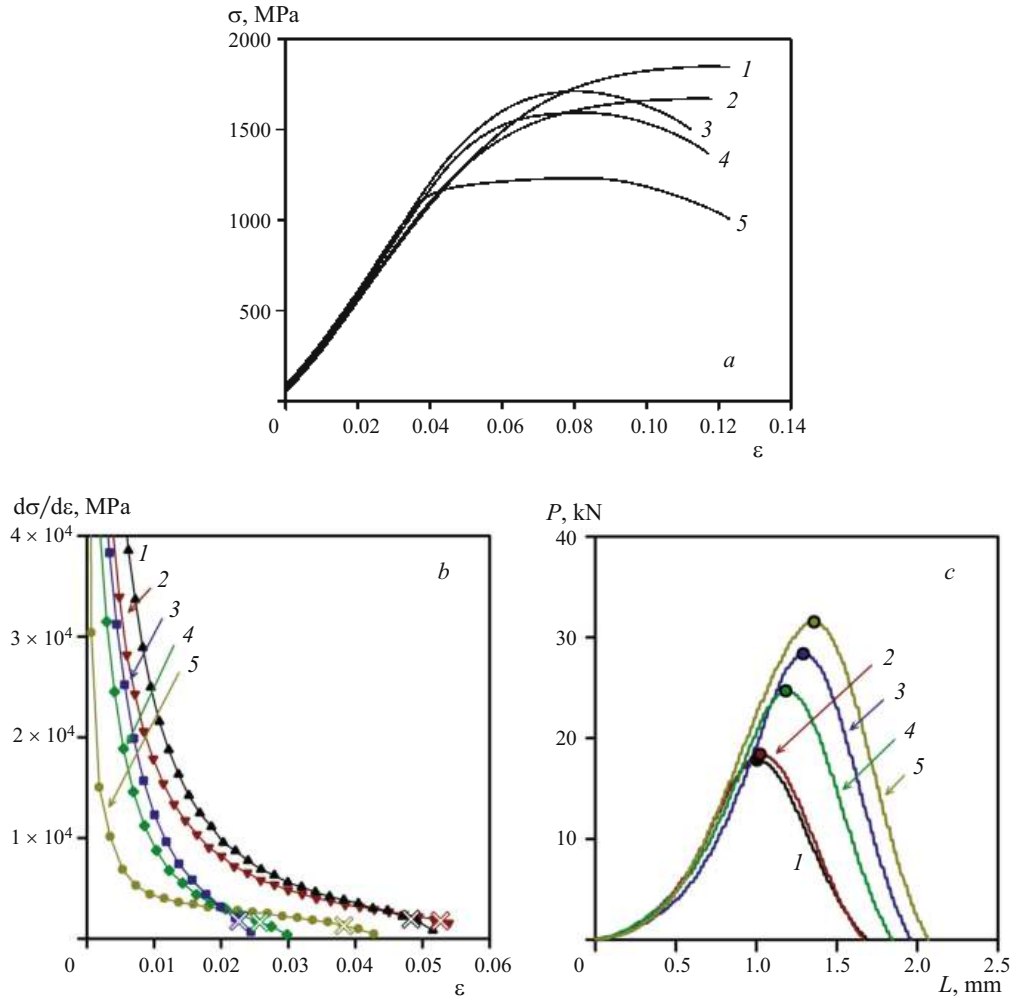
Fig. 4. Stress – strain curves (*a*), dependences of strain hardening $d\sigma/d\varepsilon$ on the degree of deformation ε (*b*) and of load *P* on the displacement *L* of the pendulum in impact toughness tests (*c*): *1*) after quenching; *2*, *3*, *4*, and *5*) after quenching and tempering at 200, 280, 400 and 500°C respectively.

where η_{Pm} is an empirical coefficient dependent on the relation between the shear and tensile stresses, P_M is the maximum load, *W* is the width of the specimen, *a* is the depth of the notch, and *B* is the thickness of the specimen. In our case, we took $\eta_{Pm} = 2.531$, because this value has been calculated for steel AISI 4340, which is close in the mechanical properties to the studied steel after quenching and low-temperature tempering [18].

It follows from Table 3 that increase of the tempering temperature promotes growth of the dynamic ultimate strength to almost an ultimate strength. After the tempering at 500°C, a critical-size crack forms only after the attainment of the ultimate strength obeying the relation $\sigma_{rd} \sim \sigma_r$, which reflects a high fracture toughness. The energy of formation of a crack E_i after the tempering at 500°C becomes almost 2.5 times higher than after the quenching. The energy of crack propagation E_p increases by only 50%. Accordingly, if the post-quenching value of E_i is about equal to E_p, it exceeds E_p by more than 80% after the tempering at 500°C.

For all the states studied, E_i is higher than E_p, and the ratio E_i/E_p increases with increase of the tempering temperature. The values of σ_{rd} are much lower than σ_r. An exception is the steel tempered at 500°C, for which $\sigma_{rd} \approx \sigma_r$.

TABLE 3. Dynamic Parameters Calculated from Load-Displacement Curves in Impact Toughness Tests

T_{temp}, °C	KCV, J/cm²	P_m, kN	σ_{rd}, MPa	E_i, J	E_p, J	E, J
Initial	13	17.8	700	5.3	4.7	10.0
200	15	18.4	720	6.7	5.6	12.3
280	19	28.3	1120	8.8	6.6	15.4
400	17	24.7	970	7.7	5.7	13.4
500	32	31.5	1240	16.2	9.1	25.3

Notations: P_m) maximum load; σ_{rd}) dynamic ultimate strength; E_i) energy of crack nucleation; E_p) energy of crack propagation; E) total absorbed energy.
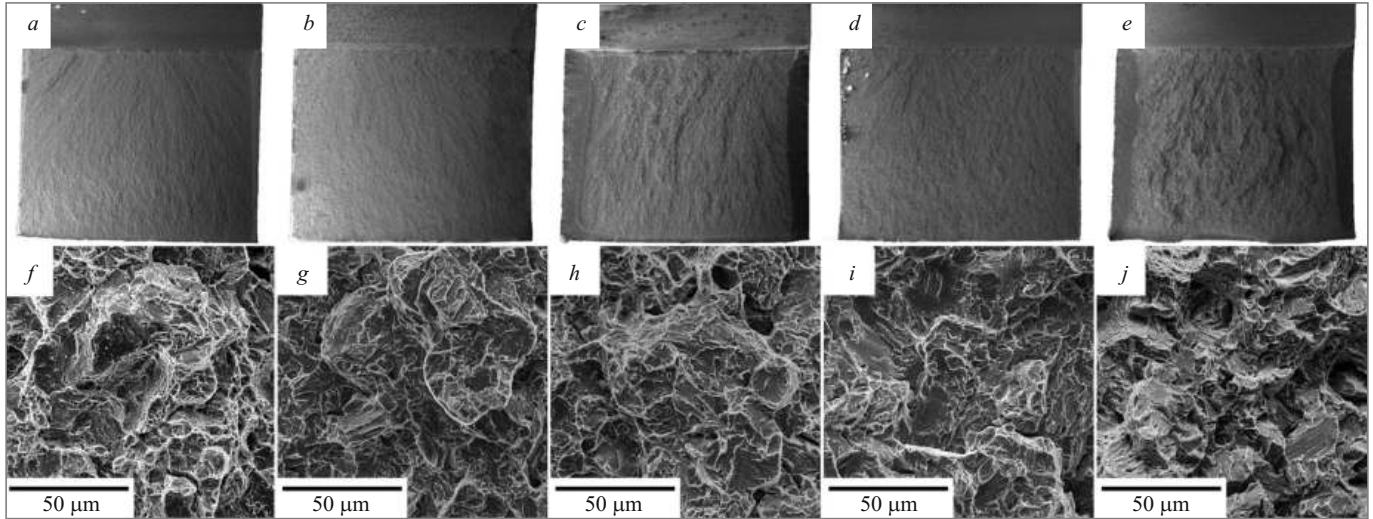
Fig. 5. Fracture surfaces (SEM) of steel specimens after quenching (e, f) and after quenching and tempering at 200°C (b, g), 280°C (c, h), 400°C (d, i), and 500°C (e, j); $f - j$) zone of rapid crack propagation; $a - d$) × 100; $f - j$) × 500.

Thus, the structure formed after tempering at 500°C provides formation of a through crack only after the attainment of a dynamic ultimate strength that corresponds to the ultimate strength under static loading.

Figure 5 presents the fractures of specimens after different treatments. After quenching, the zone of crack propagation exhibits dominance of a quasi-brittle relief represented by cleavage facets mixed with ductile detachment zones (Figs. 5a and 6f) [4, 7]. The size of the cleavage facets is comparable to that of the packets, and the detachment ridges formed at intersections of different cleavage planes $\{100\}_{\alpha'}$ exhibit dimple fracture. In addition, ductile fracture develops over the boundaries of the OAG. After the tempering at 400°C, the role of the intergrain fracture intensifies, which can be inferred from the coarser surface relief of the zone of rapid crack propagation (Fig. 5d and i). After the tempering at 500°C, it becomes well manifested, as well as the transition to cleavage within individual blocks and laths (Fig. 5e and j).

It is known that the fracture stresses σ_F for unstable crack propagation by the mechanism of cleavage are determined by the equation [21, 22]

$$\sigma_F = 1.41 \sqrt{\frac{2E\gamma_s}{\pi(1-\nu^2)}} \, d_{eff}^{-1/2}, \qquad (8)$$

where γ_s is the surface energy of the cleavage plane, $\nu = 0.293$ is the Poisson coefficient, and d_{eff} is the effective grain size.

During the tempering at 400°C, the decrease in the carbon content in the martensite raises γ_s [5, 21], which elevates σ_F and hence σ_{rd}. This promotes increase in the impact toughness.

The size of a martensite packet is assumed to be equal to the effective grain size [21], which is confirmed by the data of the fractographic analysis up to the tempering temperature of 400°C. The effective grain size d_{eff} in Eq. (7) decreases by a factor of 4 and more due to suppression of the propagation of brittle crack within martensite blocks and even laths. The depletion of the martensite with respect to carbon also raises σ_F due to the increase in γ_s. Thus, the combination of these two factors raises substantially the fracture stress σ_F and provides formation of a critical crack only when the dynamic ultimate strength is exceeded.

CONCLUSIONS

The results of the study of the mechanical properties and microstructure of steel 0.33C – 1.8Si – 1.44Mn – 0.58Cr after quenching and tempering allow us to make the following conclusions.

1. The structure of the steel after water quenching from 900°C contains fine dispersed lath martensite with lath width 180 nm. The internal elastic stresses in the steel in this condition reach 40% of the yield strength.

2. Tempering at a temperature of up to 400°C does not affect the size of the packets, but increases the width of the blocks and of the laths. Transition η-carbides precipitate in the martensite as a result of tempering at 280°C, which takes up to 90% carbon contained in the steel. Widening of the martensite laths lowers the elastic stresses, while precipitation η-carbides may cause their growth. The flow stresses grow from 1230 to 1430 MPa due to the precipitation hardening associated with formation of η-carbides in the form of plates, and the impact toughness increases due to the decrease of the carbon content in the martensite. Cementite

does not form in the steel at the tempering temperatures of up to 400°C.

3. After the tempering at 500°C, virtually all of the carbon leaves the martensite as a result of formation of chains of round-shaped cementite over the boundaries of laths and blocks. The formation of cementite causes dissolution of the transition η-carbides. The steel exhibits the following stages of carbide precipitation under tempering: martensite → η-Fe_2C → Fe_3C. The impact toughness grows both due to the decrease in the carbon content in the martensite, which raises the surface energy of cleavage planes $\{100\}_{\alpha'}$, and due to the changes in the effective grain size for the brittle fracture stresses. The yield strength remains high (1130 MPa) despite the almost total decomposition of the martensite.

4. There is no obvious correlation between the strength-ductility parameter $\sigma_r \times \delta$ (MPa · %) and the impact toughness. Tempering does not affect the value of $\sigma_r \times \delta$, while the impact toughness increases under the tempering.

REFERENCES

1. N. Fonstein, *Advanced High Strength Sheet Steels*, Springer International Publishing, New York, USA (2015), 369 p.
2. J. Zhao and Z. Jiang, "Thermomechanical processing of advanced high strength steels," *Progr. Mater. Sci.*, **94**, 174 – 242 (2018).
3. Burak Naljajy, Omer Djykhad Aidyn, Salykh Ilmaz, Volkan Kylydjly, "Effect of interrupted quenching on the microstructure, mechanical properties and dislocation density of steel AISI 4340," *Metalloved. Term. Obrab. Met.*, No. 9, 29 – 38 (2022).
4. G. Krauss, *Steels: Processing, Structure and Performance* (2005), Vol. 2, pp. 30 – 31.
5. S. Vervynckt, K. Verbeken, B. Lopez, and J. J. Jonas, "Modern HSLA steels and role of non-recrystallization temperature," *Int. Mater. Rev.*, **57**, 187 – 207 (2012).
6. Z. Xiong, P. J. Jacques, A. Perlade, and T. Pardoen, "Characterization and control of the compromise between tensile properties and fracture toughness in a quenched and partitioned steel," *Metall. Mater. Trans. A*, **50**, 3502 – 3513 (2019).
7. E. Tkachev, S. Borisov, A. Belyakov, et al., "Effect of quenching and tempering on structure and mechanical properties of a low-alloy 0.25 C steel," *Mater. Sci. Eng. A*, **868**, 144767 (2023).
8. P. B. Hirsch, A. Howie, R. B. Nicolson, et al., *Electron Microscopy of Thin Crystals*, Butterworth, London (1965), 549 p.
9. M. Calcagnotto, D. Ponge, E. Demir, and D. Raabe, "Orientation gradients and geometrically necessary dislocations in ultrafine grained dual-phase steels studied by 2D and 3D EBSD," *Mater. Sci. Eng. A*, **527**, 2738 – 2746 (2010).
10. H. Kitahara, R. Ueji, N. Tsuji, and Y. Minamino, "Crystallographic features of lath martensite in low-carbon steel," *Acta Mater.*, **54**, 1279 – 1288 (2006).
11. E. I. Galindo-Nava and P. E. J. Rivera-Diaz-del-Castillo, "A model for the microstructure behavior and strength evolution in lath martensite," *Acta Mater.*, **98**, 81 – 93 (2015).
12. V. Dudko, A. Belyakov, and R. Kaibyshev, "Evolution of lath substructure and internal stresses in a 9% Cr steel during creep," *ISIJ Int.*, **57**, 540 – 549, (2017).
13. S. Gorelik, Yu. Skakov, and L. Rastorguev, *X-ray and Optoelectronic Analysis* [in Russian], Izd. MISiS, Moscow (2002), p. 357.
14. W. Lu, M. Herbig, C. H. Liebscher, et al., "Formation of eta carbide in ferrous martensite by room temperature aging," *Acta Mater.*, **158**, 297 – 312 (2018).
15. D. Yuzbekova, A. Mogucheva, D. Zhemchuzhnikova, et al., "Effect of microstructure on continuous propagation of the Portevin – Le Chatelier deformation bands," *Int. J. Plast.*, **96**, 210 – 226 (2017).
16. P. Makarov and M. Eremin, "Interrupted yielding phenomenon as a base model for studying instabilities of deformation processes," *Fiz. Mezomekh.*, **16**, 109 – 128 (2013).
17. M. Jobba, R. K. Mishra, and M. Niewczas, "Flow stress and work-hardening behaviour of Al – Mg binary alloys," *Int. J. Plast.*, **65**, 43 – 60 (2015).
18. V. Dudko, D. Yuzbekova, S. Gaidar, et al., "Tempering behavior of novel low-alloy high-strength steel," *Metals*, **12**, 2177 (2022).
19. *ASM Handbook, Mechanical Testing and Evaluation 8*, ASM Int., New York, USA (2000), p. 2235.
20. R. Chaouadi and R. Gerard, "Development of a method for extracting fracture toughness from instrumented Charpy impact tests in the ductile and transition regimes," *Theor. Appl. Fracture Mech.*, **115**, 103080 (2021).
21. T. Hanamura, F. Yin, and K. Nagai, "Ductile-brittle transition temperature of ultrafine ferrite/cementite microstructure in a low carbon steel controlled by effective grain size," *ISIJ Int.*, **44**, 610 – 617 (2004).
22. D. Yusbekova, V. Dudko, A. Pydrin, et al., "Effect of temp-forming on strength and toughness of medium-carbon low-alloy steel," *Materials*, **16**, 1202 (2023).